Full Length Article

Initial stages of growth and electronic properties of epitaxial SrF$_2$ thin films on Ag(1 1 1)

Mauro Borghi [a], Andrea Mescola [b], Guido Paolicelli [b], Monica Montecchi [c], Sergio D'Addato [d], Simone Vacondio [c,d], Luca Bursi [d], Alice Ruini [b,d], Bryan P. Doyle [e], Tibor Grasser [a], Luca Pasquali [c,e,f,*]

[a] Institute for Microelectronics (TU Wien), Gusshausstrasse 27–29, 1040 Vienna, Austria
[b] CNR-Istituto Nanoscienze – Centro S3, Via Campi 213, Modena 41125, Italy
[c] Department of Engineering "Enzo Ferrari", University of Modena and Reggio Emilia, Via Vivarelli 10, 41125 Modena, Italy
[d] Department of Physics, Informatics and Mathematics, University of Modena and Reggio Emilia, Via Campi 213/A, 41125 Modena, Italy
[e] Department of Physics, University of Johannesburg, P.O. Box 524, Auckland Park 2006, South Africa
[f] IOM-CNR, Strada Statale 14, Km. 163.5 in AREA Science Park, Basovizza, 34149 Trieste, Italy

ABSTRACT

Molecular beam epitaxy (MBE) is used to grow ultrathin SrF$_2$ layers at different temperatures on Ag(111) epitaxial films prepared on mica. The electronic properties, structure and morphology of the films are probed by ultraviolet and x-ray photoelectron spectroscopies (UPS and XPS) supported by ab-initio calculations, reflection high energy electron diffraction (RHEED) and atomic force microscopy (AFM). The SrF$_2$ films are composed of crystallites with their [1 1 1] direction parallel to the substrate normal, thereby reproducing the symmetry of the substrate. Twinned domains are also observed. At the Ag/SrF$_2$ interface, fluoride molecules do not dissociate and the interaction with the substrate is weak. At room temperature, fluoride crystallites merge together, resulting in a continuous film covering the entire substrate when it reaches a nominal thickness of 5 nm. Growth at higher temperature induces the formation of triangular 3D islands, leaving sizable portions of the Ag substrate uncovered. At 400 °C, also a small fraction of SrF$_2$(0 0 1)-oriented crystallites are observed, with their [1 −1 0] axis rotated by about 30° with respect to the [1 −1 0] substrate direction.

1. Introduction

The introduction of new materials and architectures has always been of paramount importance in the semiconductor industry, in order to maintain a continuous reduction of the dimensions and power dissipation of the devices. Up to now, quite remarkably, Moore's law still appears to be valid. However, active regions in devices have reached the dimensions of a few nanometres, which imposes severe challenges. Difficulties include the deterioration of charge mobility, the need to introduce insulators with equivalent oxide thicknesses (EOT) below 1 nm, the reduction of power consumption and the necessity to increase durability and reliability. 2D semiconductors, for example 2D transition metal dichalcogenides (TMD) [1–4], have been recognised as very good candidates for application in next generation electronics [5]. The substitution of traditional semiconductors with 2D materials, in turn, requires the use of new types of insulators other than SiO$_2$ in fundamental

architectures like field effect transistors (FET). This is demanding, since appropriate dielectrics require a wide bandgap, a low density of defects at the interface and inside the films, which act as charge traps or preferential paths of leakage current, a high dielectric constant, as well as high breakdown fields. Recently, ionic fluorides have been suggested as favourable dielectrics [6–8] compared to most oxides, including high-k [9] and layered insulators, like hexagonal boron nitride (h-BN) [10]. When grown at moderate temperature on Si(111) [11,12], CaF$_2$ forms flat and pinhole-free layers that are (1 1 1) oriented and F terminated. This guarantees interface passivation, low defect density and van der Waals interaction with 2D semiconductors, suggesting that ultrathin fluorides can behave as almost ideal insulators for 2D based devices. FETs with promising electrical behaviour have indeed been fabricated [8]. To move forward towards viable applications, the preparation of ultrathin fluoride layers on conductive (i.e., metallic) contacts, which work more effectively as gate contacts compared to Si(111) substrates,

is required. While the growth of fluorides on silicon has been studied quite extensively in the past [13–21], the growth modes on metals have been scarcely investigated up to now. To cite a few relevant examples, Calleja *et al.* [22] reported the epitaxial growth of CaF$_2$(111) on Cu (111) investigated by scanning tunnelling microscopy (STM) and low energy electron diffraction (LEED) as a function of the substrate temperature, while Farìas *et al.* [23] observed a novel nucleation mechanism of LiF on Ag(111) involving nucleation at the step edges between adjacent terraces.

This work aims at extending the knowledge about the growth modes of fluorides on metals and, in particular, the growth of ultrathin SrF$_2$ layers on Ag(111) by molecular beam epitaxy (MBE), focussing on the interface formation and initial film structure and morphology. SrF$_2$ is similar to CaF$_2$, with which it shares the same crystal cubic Fm$\bar{3}$m structure. The two materials present similar optical and dielectric properties. Both of them can be evaporated in molecular form directly in ultra-high vacuum (UHV) and both fluorides have been largely studied in the form of ultrathin nanocrystalline layers on semiconductors. In the present case, we have chosen SrF$_2$ instead of CaF$_2$ or BaF$_2$ because of its lattice parameter in relation to Ag(111) (lattice parameters of CaF$_2$, SrF$_2$ and BaF$_2$ are 5.46 Å, 5.80 Å and 6.20 Å, respectively, while for Ag it is 4.09 Å). In spite of the mismatch of the cubic lattice constants of the metal and SrF$_2$, the misfit reduces to about 0.4 % when considering the spacing between two Ag atoms along the [110] direction and the spacing between two Sr atoms along the [100] direction. Furthermore, the thermal expansion coefficient of the two materials is similar: 1.8–1.9 $\times 10^{-5}$ K^{-1} at room temperature. Therefore, it could be expected that epitaxial growth is favoured for SrF$_2$ with respect to the other fluorides.

SrF$_2$ has been deposited in UHV by molecular beam epitaxy at different substrate temperatures, from room temperature (RT) to 400 °C, on Ag(111). As substrates, we used thin single-crystalline Ag(111) films deposited on flat mica supports. On the one hand, Ag(111) films deposited on mica guarantee a very high quality, comparable to bulk single crystals [24], and they have been already adopted successfully in a number of studies related to the growth of thin films on Ag(111) [25–27]. On the other hand, in perspective, this type of support makes it viable the fabrication of devices directly on an almost ideal Ag(111) surface, which would be hardly feasible with a bulk single crystal. In fact, it should be considered that while single crystals are ideal for fundamental studies, they are not suitable for the fabrication of layered devices, as it would be for a MISFET structure. Ag/mica can represent a nice solution to address both aspects.

Electronic properties have been probed by x-ray and ultraviolet photoemission (XPS and UPS) supported by ab initio calculations of the surface, interface and bulk densities of states (DOS). Structural and morphological information were investigated by atomic force microscopy (AFM) ex-situ and reflection high energy electron diffraction (RHEED) in-situ. The growth mode is influenced by the substrate temperature: results show that by increasing the deposition temperature from RT to 400 °C, the growth mode of the fluoride film changes from uniformly covering the substrate to three-dimensional (3D) islands that leave parts of the silver surface uncovered.

2. Material and methods

2.1. Experimental

SrF$_2$ on Ag(111) was grown by MBE in UHV conditions (chamber base pressure 2 × 10^{-10} mbar). Different nominal thicknesses were studied, namely 0.5, 1.5, 5, 10 and 15 nm, and growth was carried out at different substrate temperatures: RT, 250 °C and 400 °C.

In order to evaporate the strontium fluoride, a Knudsen cell [21] with a graphite crucible loaded with strontium fluoride crystals (MSE Supplies LLC, purity 99.99 %) was used. The crucible was heated by a tungsten filament up to about 1100 °C to produce the molecular beam. The base pressure in the chamber during evaporation was in the 5–9 ×

10^{-9} mbar range. The growth rate was calibrated with a quartz micro balance positioned in proximity of the sample and set at 0.2 nm/min. The evaporation rate was kept constant for all samples and all coverages. The rate was controlled before and after each deposition step with the quartz micro balance.

As substrates, epitaxial 300 nm-thick films of Ag(111) grown on mica (purchased from Mateck GmbH) were used, cleaned in situ through Ar$^+$ sputtering cycles (1 kV, 1 μA, 5 min) and annealing at 520 °C (15 min). This guarantees a surface quality comparable to the one of a bulk single crystal [24]. The substrates were heated indirectly by passing current through a tungsten filament positioned in proximity behind the sample holder plate. The temperature was measured with a K-type thermocouple connected to the sample holder plate. Surface cleanliness was assessed by UPS, XPS as well as electron diffraction – RHEED – through the inspection of the valence band, the core levels and the diffraction patterns of both the bare substrate and the fluoride films. UPS, XPS as well as RHEED were taken in-situ directly after growth, in the same vacuum vessel used for MBE. The UHV vessel includes different sections: one is dedicated to film growth, hosting the evaporation cell and the RHEED system; the other is dedicated to spectroscopy.

RHEED patterns were recorded after each deposition step with a Perkin-Elmer model 06–190 electron gun operated at 10 keV and at 2° of grazing incidence. The RHEED screen was positioned at a distance of 108 mm with respect to the electron gun spot at the centre of the sample. The crystal structure and the epitaxial relations were derived from the diffraction patterns with the support of the Rec Space code developed by S. Suturin et al. [28]. Morphological information was obtained ex-situ using an Atomic Force Microscope (AFM) NT-MDT, NTEGRA AURA system. The AFM was operated in semi-contact mode and measurements were performed in air, under ambient conditions (T ≈ 25 °C, relative humidity ≈ 55 %) using commercially available rectangular shaped silicon cantilevers with nominal elastic constants between 0.3 and 0.8 N/m (MikroMasch HQ:CSC37/NoAl).

Photoemission spectra were taken with an Omicron EA125 electron analyser at normal emission. For UPS, He I photons ($h\nu$ = 21.2 eV) were used from a windowless differentially pumped Vacuum Generators UV discharge lamp and with a resolution of 50 meV. XPS was carried out with non-monochromatic Al K_α photons ($h\nu$ = 1486.6 eV) from a Vacuum Generators XR3 dual anode source operated at 15 kV, 18 mA and with a resolution of 1 eV for wide overview spectra and 0.5 eV for single peak line-shape analysis. All spectra were recorded at RT, allowing the samples to cool down before the measurements. Binding energies are referenced to the Fermi energy of the silver substrate. XPS spectra are reported after removal of the x-ray source satellites and a Shirley background subtraction.

2.2. Calculations

Ground-state electronic structure simulations and geometry optimizations for the SrF$_2$ and Ag bulk systems, the SrF$_2$(111) and Ag(111) slabs to model surfaces, and the SrF$_2$/Ag(111) interface were performed by using a state-of-the-art first principles atomistic total-energy and forces approach based on Kohn–Sham (KS) density-functional theory (DFT) [29–31], as implemented in the Quantum-ESPRESSO package [32,33]. All calculations employed the Perdew-Burke-Ernzerhof (PBE) generalized gradient approximation (GGA) to the exchange–correlation (xc) functional [34], a plane wave basis set with a kinetic energy cutoff of 120 Ry (480 Ry) for the description of KS wave functions (charge density), and optimized norm-conserving Vanderbilt pseudopotentials (ONCVPSP) to account for atomic potentials [35]. The Brillouin zone (BZ) of bulk SrF$_2$, bulk Ag, and the SrF$_2$/Ag(111) interface was sampled with (4 × 4 × 4), (12 × 12 × 12), and (4 × 4 × 1) uniform meshes of **k**-points, respectively. The two-dimensional BZs of the slab systems were sampled with meshes consistent with those used in the bulk systems. For Ag, a gaussian smearing parameter of 0.01 Ry was used.

Both SrF$_2$ and Ag bulk systems are characterized by face-centred

cubic (fcc) structures described by the Fm̄3m space group, with one Sr atom and two displaced F atoms per lattice point in the former, and one Ag atom per lattice point in the latter. The surfaces were simulated by building supercells including a slab and at least 15 Å of vacuum to separate periodic replicas in the direction perpendicular to the considered surface. The supercell for the SrF_2/Ag(1 1 1) interface was constructed by considering that the lattice parameter of Ag is approximately two-thirds of the one of SrF_2 and stacking 10 layers of Ag(1 1 1) and 7 layers of SrF_2(1 1 1) along the vertical direction.

The bulk SrF_2 structure was fully relaxed using different energy cutoffs and **k**-point grids. The lattice parameter was found to converge with a 120 Ry cutoff and a $4 \times 4 \times 4$**k**-point grid, giving a = 11.057 a.u. The density of states (DOS) was then computed, including its projections (PDOS) on KS orbitals for the characterization of the peaks.

All structures were relaxed under the effect of the interatomic forces, until forces on all atoms were lower than 0.003 eV·Å^{-1}. In addition, bulk cells and interface supercells were relaxed until the pressure was lower than 0.5 kbar. After fully relaxing the SrF_2/Ag(1 1 1) supercell, the equilibrium distance between the Ag(1 1 1) and SrF_2 (1 1 1) slabs was 3.7 Å. The equilibrium lattice parameters obtained for SrF_2 and Ag bulk systems were 5.85 Å and 4.15 Å, respectively, which deviate by less than ~ 2 % from the relative experimental values [36]. On the other hand, the KS band gap of SrF_2 obtained from our simulations using the PBE xc functional was 6.83 eV, which underestimates by ~ 40 % the experimental value [37–39]. Furthermore, the onset of the strong 4d band contribution of Ag to the density of states (DOS) is predicted by PBE to be ~ 2.6 eV below the Fermi energy, which is not in good agreement with the UPS spectra of the present work. The use of a hybrid xc functional provides results closer to the experimental values, but at a significantly greater computational cost, especially when a plane-wave basis set is employed [40]. As an accuracy test, we simulated the electronic properties of bulk SrF_2 and of the SrF_2/Ag(1 1 1) interface with a hybrid HSE xc functional. We obtained a *quasi*-rigid shift of the valence band in the bulk HSE DOS (not shown), resulting in a band gap of 8.91 eV, only 21 % smaller than the experimental one [41]. The 4d onset of Ag was found to be at ~ 3.8 eV below the Fermi energy, also in better agreement with experimental data (including the UPS spectra of the present work). While HSE introduced important quantitative improvements, qualitative agreement with the PBE results for the DOS was preserved. Therefore, the PBE level of theory suffices for the characterization of the experimental findings of Section 3.2.1, at a reduced computational cost with respect to HSE.

The DOS was calculated from the electronic structure of each system in order to characterize the features in the UPS spectra. Calculations included projections on pseudo-atomic wavefunctions (PDOS) localized on different atomic layers (layer-resolved), particularly the ones closer to the interface. In order to align features in the DOS of the SrF_2/Ag (1 1 1) interface with the experimental UPS spectra, we computed the ionization potential (IP) of SrF_2(1 1 1) and the work function ϕ of Ag (1 1 1). A vacuum region of thickness ~ 20 Å was used in the slab supercells, and the KS potential was computed along the [1 1 1] direction and averaged in the perpendicular plane [42]. The value of the averaged potential in the vacuum region where flatness was attained was identified as the vacuum energy ε_{vac}. The ionization potential was then computed, at the PBE level, as IP = ε_{vac} - ε_{HOMO}, with ε_{HOMO} being the energy of the KS highest-occupied molecular orbital (HOMO). Analogously, the work function was computed as ϕ = ε_{vac} - ε_{Fermi}, with ε_{Fermi} being the Fermi energy of the system [43,44]. The values of IP and ϕ converged when using 10 SrF_2 and 14 Ag(1 1 1) planes, respectively, resulting in IP = 7.77 eV and ϕ = 4.35 eV. While the latter is in reasonable agreement (~6% underestimation) with our experimental value of 4.5 eV, the former is underestimated consistently with the underestimation of the band gap due to the adopted PBE-GGA xc functional [45].

Concerning the alignment of the PDOSs of the SrF_2/Ag(1 1 1) interface, our numerical evidence suggests that interfacing two slabs of SrF_2

and Ag in the simulation supercell tend to align the vacuum levels that the two slabs would have had if separate. This is however not what is observed in UPS. Agreement is recovered by referring the PDOS of SrF_2 to the calculated ε_{vac} of an isolated SrF_2 slab, and the PDOS of Ag to either the Fermi energy of the SrF_2/Ag(1 1 1) interface or the Fermi energy of Ag alone. Therefore, these energy references were adopted for the PDOSs shown here, for comparison with the experiment.

3. Results

### 3.1. Structure and morphology

3.1.1. Clean Ag(1 1 1)
Fig. 1a shows an AFM image of a typical clean Ag(1 1 1) surface, taken before the deposition of strontium fluoride and after the sputtering and annealing cycles. The image shows the presence of terraces separated by atomic steps, typical of Ag(1 1 1) [46]. Some small white protrusions that show up at step edges are ascribed to debris or traces of physisorbed contaminants due to the exposure to air during AFM imaging. Assignation of these features to some level of contamination while the sample is in vacuum after cleaning are excluded on the basis of XPS (see below). The width of the terraces varies from ~ 30 nm to ~ 200 nm. Fig. 1b displays the diffraction pattern of the same silver surface before air exposure, with the electron beam directed along the [1 −1 0] crystallographic direction of the (1 1 1) plane. The distances and shapes of the modulated streaks of the diffraction pattern are compatible with a multi-stepped surface as observed by AFM. Kikuchi lines due to electron scattering in the Ag crystal are also present.

3.1.2. Room temperature growth
Fig. 2a displays the Ag(1 1 1) surface morphology after the growth of 0.5 nm of strontium fluoride at RT. The AFM image shows a dendritic-like growth of the film, which has been observed previously for other fluorides grown on metals [22,23,47]. The AFM phase contrast image (Fig. 2b) suggests a surface composed of two different materials, one of which is the area unoccupied by the dendritic fluoride islands which remains clean, uncoated silver (see also below, section 3.2.1). The RHEED diffraction pattern taken with the electron beam along the [1 −1 0] direction (Fig. 2c) confirms this picture. It shows groups of double streaks relative to first-order diffraction rods (and partially to second-order) associated with the silver (1 1 1) surface reciprocal lattice periodicity perpendicular to the [1 −1 0] direction (evidenced with black marks in Fig. 2c) and to the periodicity of the SrF_2(1 1 1) plane (red marks in Fig. 2c) that grows mimicking the substrate geometry. The modulation of the streaks is coherent with the presence of islands, as observed by AFM. Therefore, SrF_2 islands tend to grow with their [1 1 1] direction perpendicular to the substrate. This is consistent with the fact that (1 1 1) planes of fluorides present the lowest surface free-energy [13]. Moreover, from the measured distance between the diffraction streaks, SrF_2 appears to be strain-relaxed to its bulk lattice parameter from the initial growth phases, with crystallographic directions aligned to those of the substrate and preserving its rotational symmetries.

The modulation of the streaks is even more evident from the electron diffraction performed on the film at 1.5 nm of nominal coverage, Fig. 2d, where the diffraction from the substrate is no longer visible, and at 5 nm, Fig. 2g. A simulation of the RHEED pattern obtained with the Rec Space code [28] suggests the presence of two twinned domains of the fluoride lattice, rotated at 180° to each other with respect to the substrate. The simulation of the diffraction from the two domains is marked in the RHEED figures with red and green open circles, respectively.

The absence of the pattern of Ag(1 1 1) already at 1.5 nm indicates that the fluoride islands have coalesced and cover the whole substrate. This is confirmed by AFM (Fig. 2e-f) which shows, in particular due to the uniformity of the phase-contrast image (Fig. 2f), that only one material is present at the surface. In addition, the surface topography (Fig. 2e) shows brighter aggregates (protrusions) in the form of thin
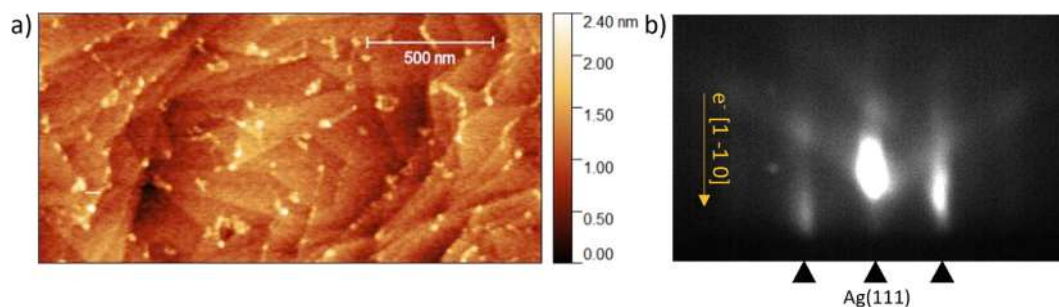
Fig. 1. a) Ex-situ AFM image of Ag(1 1 1) substrate after sputtering and annealing, where the terraces of the Ag(1 1 1) are clearly visible. b) RHEED pattern of the silver substrate. The position of the Ag(1 1 1) diffraction rods have been indicated. The electron beam is directed along the [1 −1 0] Ag surface direction.

irregular lines that can be associated with some degree of fluoride island decoration at the steps, already apparent at 0.5 nm of coverage, in agreement with analogous observations for CaF_2 on Cu(1 1 1) [22]. Besides this, some degree of accumulation of debris at step edges during air exposure in AFM imaging cannot be excluded.

3.1.3. High - temperature growth

Fig. 3a shows an AFM image of a 5 nm thick film of SrF_2 grown with the Ag(1 1 1) substrate held at 250 °C. The morphology of the film has changed compared to the one deposited at RT. The film grows now into regular structures, with a base width between 50 and 130 nm and a height between 2 and 8 nm. The fluoride islands do not appear to be coalesced into a uniform film, contrary to the RT case. The islands appear to be pyramidal huts, consistent with a stacking of horizontal (1 1 1) oriented layers. The facets of the pyramids are therefore not smooth but present stepped terraces. The RHEED pattern confirms the crystallinity of these structures, showing modulated streaks due to surface morphology and are also compatible with two specular orientations of the SrF_2(1 1 1) lattice, rotated by 180° from each other. This is emphasised in Fig. 3b, where the superposition of the simulation of the diffraction spots due to the two domains is shown as red and green circles.

Fig. 4a shows an AFM image (and Fig. 4b the corresponding phase contrast) of a 5 nm film of SrF_2(1 1 1) grown with the substrate held at 400 °C. It shows triangular-shaped islands, relatively flat on top with heights between 6 and 7 nm. The islands are larger than those obtained at 250 °C and do not show a pyramid-like structure, but rather a prismatic shape, with a triangular base. There are clearly two main orientations of the triangular islands, specularly rotated by 180°, consistent with the twinned structures.

RHEED (Fig. 4c) confirms the (1 1 1) vertical orientation of the islands. Interestingly, the RHEED pattern, in addition to the streaks belonging to the SrF_2(1 1 1) crystal lattice (modelled with red circles), also shows alternating spots on the sides of the main streaks. These spots are assigned to diffraction due to differently-oriented SrF_2 islands. According to the model (green circles), this diffraction pattern seems to result from SrF_2(0 0 1)-oriented crystallites, with their [1 −1 0] axis rotated by about 30° with respect to the [1 −1 0] direction of the substrate. This epitaxial relation may possibly be associated with the 'smaller' and 'higher' islands that show up as brighter spots in the AFM image of Fig. 4a and that look almost square in shape. Therefore, basically two types of the epitaxial relations may be inferred: a dominant one corresponding to SrF_2(1 1 1)||Ag(1 1 1) and SrF_2[1 −1 0] (R0° and R180°)||Ag[1 −1 0], and a minor one corresponding to SrF_2(0 0 1)||Ag (1 1 1) and SrF_2[1 −1 0] R30°||Ag[1 −1 0].

3.2. Electronic properties

The chemical composition and interface reactions, together with information on band alignment, were obtained by photoelectron spectroscopy. In particular, UPS was used to investigate the evolution of the valence states as a function of the nominal thickness and growth temperature, while XPS was used to access core levels of both the substrate and the overlayer. DFT was used to calculate the valence band density of states of the SrF_2/Ag(1 1 1) system to compare with the experiment and guide in the assignment of the spectral features.

3.2.1. Room temperature growth

Fig. 5 shows the UV-excited electron distribution curves of the valence band as a function of the electron binding energy at different nominal coverages and deposited at RT. The spectrum of the clean surface is dominated by the emission from the 4d band of Ag(1 1 1) between 4 and 8 eV, with contributions from sp states. States of sp character determine the emission below 4 eV, down to the Fermi level [48,49].

As soon as SrF_2 is deposited on the surface, the broad emission due to the fluoride F 2p valence band gradually increases, centred at about a binding energy of 8–9 eV. Correspondingly, the structures associated with the substrate progressively reduce in intensity. Surprisingly, apart from a reduction of the intensity, the line shape of the features associated with the clean Ag(1 1 1) surface persist almost unvaried up to 1 nm of nominal coverage. This is consistent with observations by AFM and RHEED, with sizable portions of the surface remaining uncovered by the fluoride. Above 1 nm the Ag structures are strongly suppressed and they are no longer visible at 5 nm. At this stage, AFM shows that the surface is completely covered with a fluoride film.

Besides the strong emission with a maximum at 8–9 eV, the fluoride film at 5 nm presents a low binding energy tail extending to about 4 eV. This has been observed previously also for SrF_2 deposited on Si [21] and on InP [50]. It is associated with the interface or surface contributions of the F 2p states. The line-shape of the valence band does not suggest any chemical reaction occurring between SrF_2 and Ag.

It is noteworthy that further deposition does not change the lineshape of the F 2p band appreciably, indicating that the electronic structure of the film has reached saturation, typical of bulk SrF_2. A rigid shift of the entire structure towards higher binding energies is instead observed. This has also been observed in previous studies of fluorides on semiconductors [21,51]. At very low coverage, the low binding energy position of the F 2p emission can be related to the effect of the screening of the metal electrons on the electron hole produced during the photoemission process in the fluoride, in proximity of the interface. At higher coverage, when screening from the substrate is largely absent, the description of the energy shift towards higher binding energy requires some argumentation, and it will be addressed below, when discussing an analogous effect occurring on the XPS peaks of the fluoride.

Besides the energy shift of the F 2p structure, the persistence of the low binding energy tail even at high coverage supports its assignment as a surface-related effect and not due to the buried interface.

In Fig. 6 the calculated bulk and layer-resolved (P)DOSs of the individual materials and of the interface between SrF_2(1 1 1) and Ag(1 1 1) are presented. In particular in Fig. 6a, the PDOSs of the two individual materials are shown. It should be noted that the relative positioning of
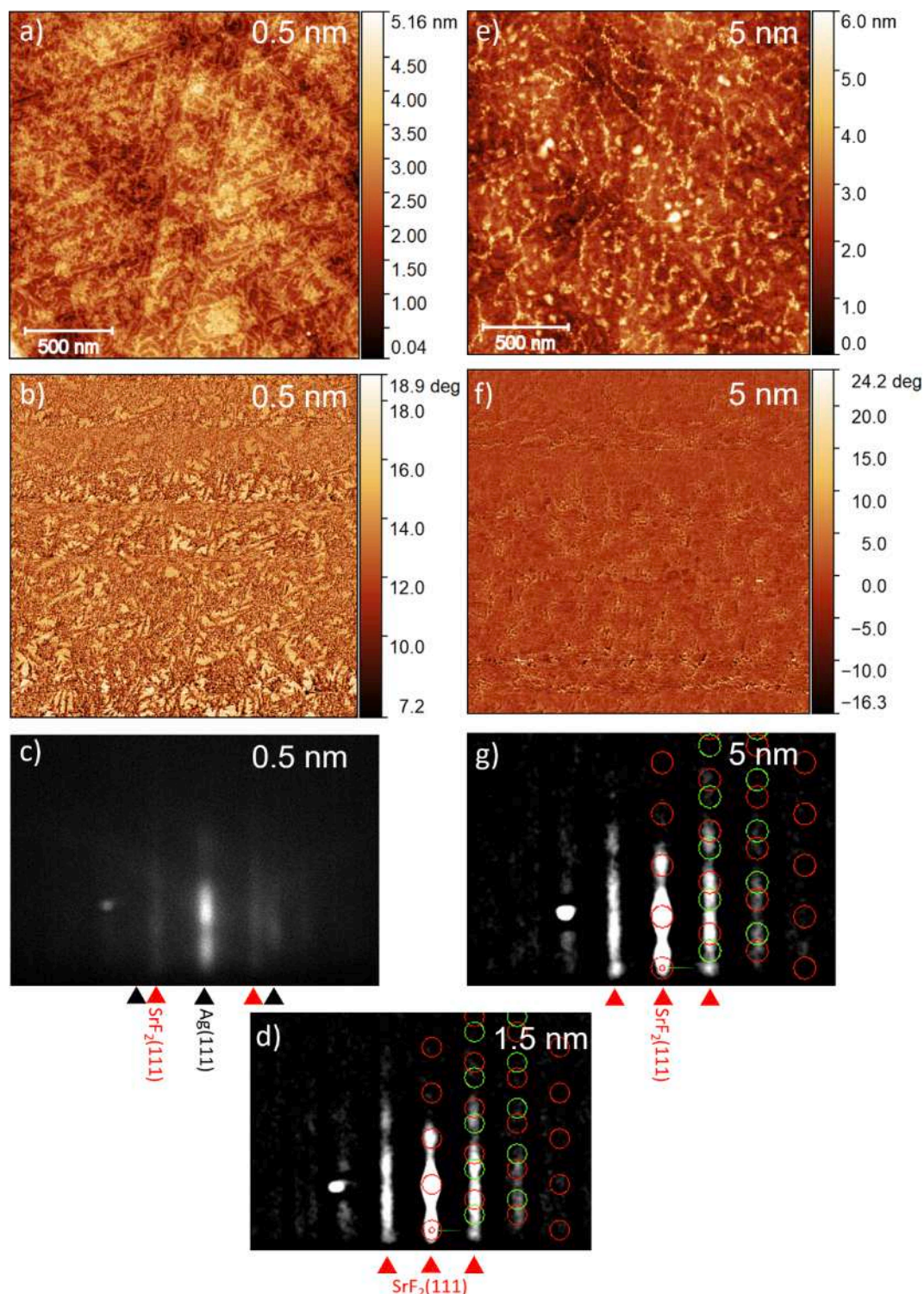
Fig. 2. a) Ex-situ AFM image (2 × 2 μm) after the deposition of 0.5 nm of SrF$_2$ at RT in morphology contrast; b) phase contrast of a); c) RHEED pattern corresponding to 0.5 nm of SrF$_2$ grown at RT, with the electron beam along the [1 −1 0] direction; d) RHEED pattern corresponding to 1.5 nm of SrF$_2$ grown at RT with the electron beam along the [1 −1 0] direction; e) Ex-situ AFM image (2 × 2 μm) after the deposition of 5 nm of SrF$_2$ at RT; f) phase contrast of e); g) RHEED pattern after the deposition of 5 nm of SrF$_2$ grown at RT, with the electron beam along the [1 −1 0] direction. In RHEED patterns, the positions of the Ag(1 1 1) and SrF$_2$(1 1 1) surface diffraction rods have been indicated with black and red arrows, respectively. The simulation of the diffraction spots due to two SrF$_2$ (1 1 1) domains oriented at 180° to each other is also shown as red and green circles [28]. (For interpretation of the references to colour in this figure legend, the reader is referred to the web version of this article.)
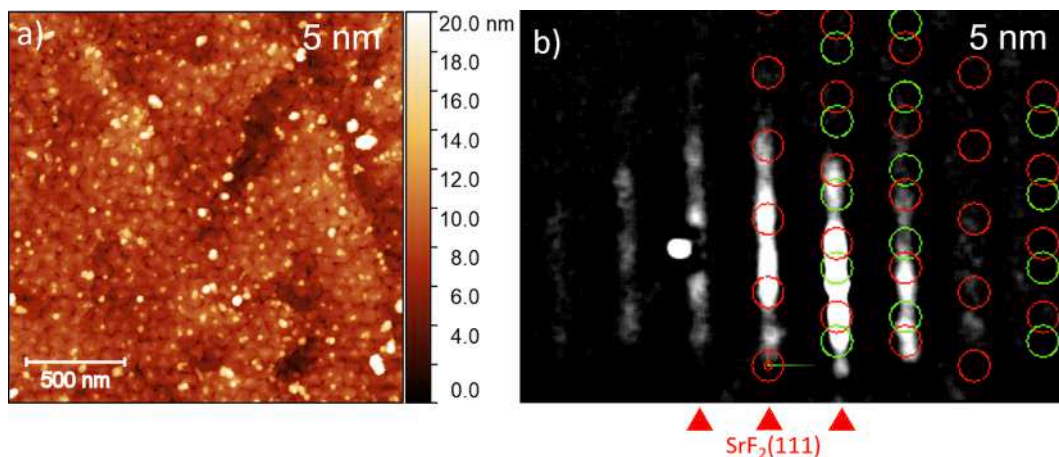
Fig. 3. a) Ex-situ AFM image (2 × 2 μm) after the deposition of 5 nm of SrF_2 at 250 °C. b) RHEED pattern corresponding to 5 nm of SrF_2 grown at 250 °C, with the electron beam along the [1 −1 0] direction. The simulation of the diffraction spots due to two $SrF_2(111)$ domains oriented at 180° to each other is shown as red and green circles [28]. In RHEED pattern, the position of the $SrF_2(111)$ surface diffraction rods has been indicated with red arrows. (For interpretation of the references to colour in this figure legend, the reader is referred to the web version of this article.)
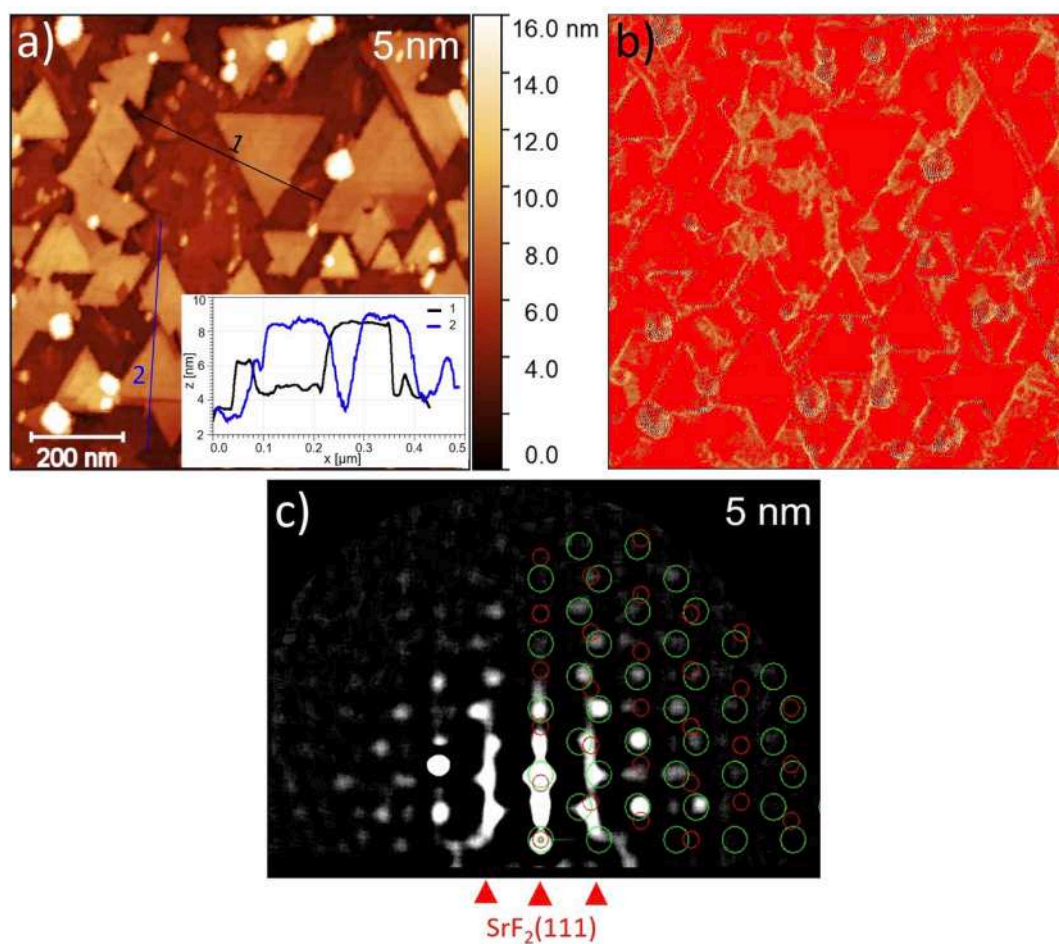
Fig. 4. a) ex-situ afm image (1 × 1 μm) after the deposition of 5 nm of SrF_2 at 400 °C. The height profile of the islands is shown in the inset for the two lines indicated in the AFM image. b) phase contrast of a). c) Experimental and modelled RHEED patterns after the deposition of 5 nm of SrF_2 grown at 400 °C, with the azimuth along the [1 −1 0] direction. The green circles stand for the SrF_2 (0 0 1) lattice orientation, rotated by 30°, while the red ones match the SrF_2 (1 1 1), also marked with red arrows. (For interpretation of the references to colour in this figure legend, the reader is referred to the web version of this article.)

the F 2p bands and of the Ag bands differs in the calculated DOS from how it is in the experimental UPS spectra. The energy scale of the SrF_2 and Ag PDOSs was respectively adjusted in order to match the peak

ordering of the experimental spectra. It can be noticed from Fig. 6a that the fluorine layer-resolved PDOSs of the surface layers are significantly shifted towards lower binding energy compared to the bulk (see in
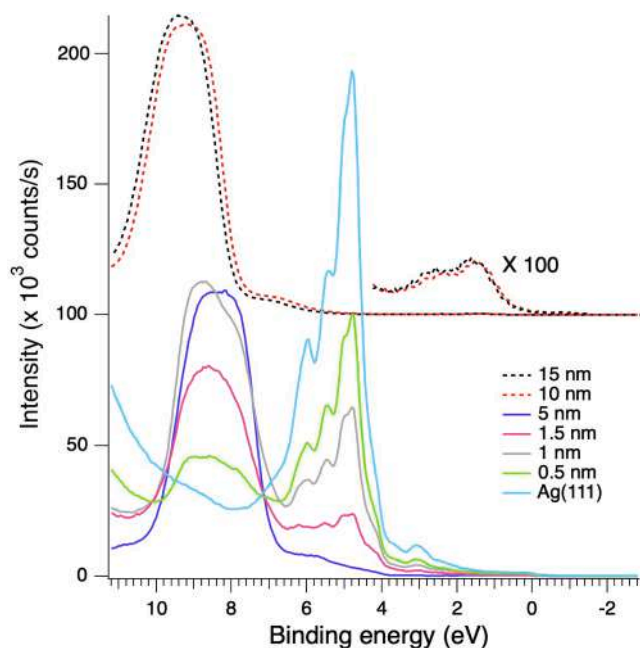
Fig. 5. UPS spectra recorded at normal emission as a function of SrF$_2$ thickness and deposited at RT. The spectra acquired at 10 and 15 nm of nominal thickness are also shown, shifted vertically by 100 kCounts/s for clarity.
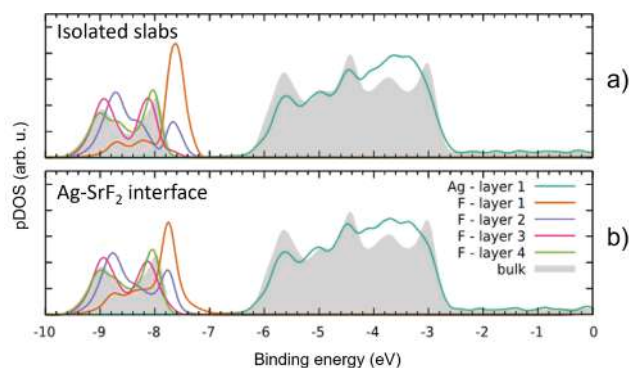
Fig. 6. Computed layer-resolved PDOS projected on pseudo-atomic wave-functions of (a) isolated SrF$_2$(1 1 1) and Ag(1 1 1) slabs and (b) the SrF$_2$/Ag (1 1 1) interface. Layer 1 of either slab is (a) the surface layer or (b) the layer at the interface; the other layers are progressively deeper according to the numbering. Bulk PDOSs are also shown in grey for reference. The PDOSs of F and Ag have two different references in the energy scale as detailed in Section 2.2.

particular layer 1 and partially layer 2). This suggests that the low binding energy tail of the experimental F 2p band can be traced back to surface contributions. Looking at Fig. 6b, which shows the evolution of the projected DOS when the two materials are combined to form the interface, one may also infer that this tail is enhanced by the presence of the interface. Indeed, here the F 2p peak of layer 1 loses some spectral weight to a low binding energy tail. No other relevant modifications are found in the comparison with the isolated slabs. On the one hand, this means that the buried interface also presents a shifted F 2p component with respect to the bulk. On the other hand, this indicates that there are no chemical bonds forming between the two slabs and hence the two materials interact weakly, as also suggested by the analysis of the system's configuration after structural relaxation. In such a case, the equilibrium distance between the Ag(1 1 1) and SrF$_2$(1 1 1) slabs is 3.7 Å, on average, which is greater than the distances between (1 1 1) layers in both constituent systems.

Fig. 7 displays the evolution of the core levels of the films as measured by XPS. Wide scans (Fig. 7a) show the progressive increase of Sr and F related peaks, together with the attenuation of the features related to Ag. No traces of carbon or oxygen contamination are present. At 15 nm of nominal coverage, faint contributions from the Ag 3d states are still visible. Taking into account that the inelastic mean free path of Ag 3d photoelectrons excited by photons of 1486.6 eV in the fluoride is < 3 nm [52], this clearly indicates that the fluoride film is not uniformly thick and 3D growth is present. Ag 3d levels are reported at higher resolution in Fig. 7b. The line shape and energy position of the structures does not vary with coverage and no chemical shifts are detected. An estimation of the effective thickness on the basis of the attenuation of the Ag 3d peaks is not attempted in the present case, since it is evident that the growth is not planar at high coverage and the procedure would therefore give unreliable results.

The stoichiometric ratio between Sr and F, as evaluated from the peak areas of Sr 3d and F 1s levels weighted by the relative atomic sensitivity factors, corresponds to the bulk SrF$_2$ composition from the early deposition stages. This proves that fragmentation of the molecules does not occur.

Sr 3d peaks are shown in Fig. 7c. At low coverage (0.5 and 1.5 nm) the spectrum has been fitted with two Voigt doublets, accounting for the spin–orbit splitting between 3d$_{5/2}$ and 3d$_{3/2}$ states of 1.8 eV. The low binding energy component is associated with Sr at or close to the interface, which are screened by the substrate metallic electrons. The higher binding energy component, whose intensity progressively increases with thickness, is associated with Sr atoms in a 'bulk-like' configuration. At 5 nm of nominal coverage and above, the bulk-like Sr component is the only one present, which is why the fits have only one component. A single peak is observed also for F 1s at all investigated thicknesses (Fig. 7d). The shift towards higher binding energy at progressively increasing coverage is also present here.

It is noteworthy that the Sr 3d peak (Fig. 7c), as well as the F 1s structure (Fig. 7d) and the F 2p band (Fig. 5) are affected by the same progressive shift towards higher binding energies of about 1.2 eV. We exclude that this is due to charging in the film, since the Ag 3d levels do not show any variation of the binding energy. Weiss et al. [50] have noted a similar trend in the case of CaF$_2$ and SrF$_2$ grown on InP and they explained this in terms of the development of a potential drop along the thickness of the film, due to the mobility of interstitial fluorine ions, generated from Frenkel pairs in the fluoride, towards the buried interface, with a consequential downward variation of the energy levels of the insulator. But in their case, the long diffusion lengths of the fluorine ions needed to reach the interface were justified by the fact that their films were grown at high temperature. At RT growth, the mobility and diffusion length would not be sufficient to generate the observed potential drop. Alternatively, irradiation by ultraviolet or x-ray photons at high flux or by electronic beams is well known to produce fluorine vacancies at the surface [53,54]. In this case, surface fluorine vacancies induce the generation of a partially filled band in the insulator gap that shifts downwards the energy levels [54]. In our case, irradiation doses would not be sufficient to explain the effect. Moreover, also RHEED patterns were recorded using very low doses at low electron current (few nA), to avoid irradiation damage. Instead, we tend to ascribe the downward shifts of the levels to the defects (i.e., filled fluorine vacancies) that are created during the progressive growth of the film, which is three-dimensional, as noted above. Defects, especially at step edges and at boundaries between merging crystallites, can produce an effect similar to the one observed during irradiation, that is the formation of filled electronic states in the gap inducing a bending of the bands. The evidence of this is shown in Fig. 5, where the spectra of the 10 and 15 nm films have been magnified by a factor of 100 and show the development of a band of filled states just below the Fermi energy position of the metal.

Overall, the core levels of the substrate and of the overlayer confirm that a strong chemical bonding is not occurring at the interface.
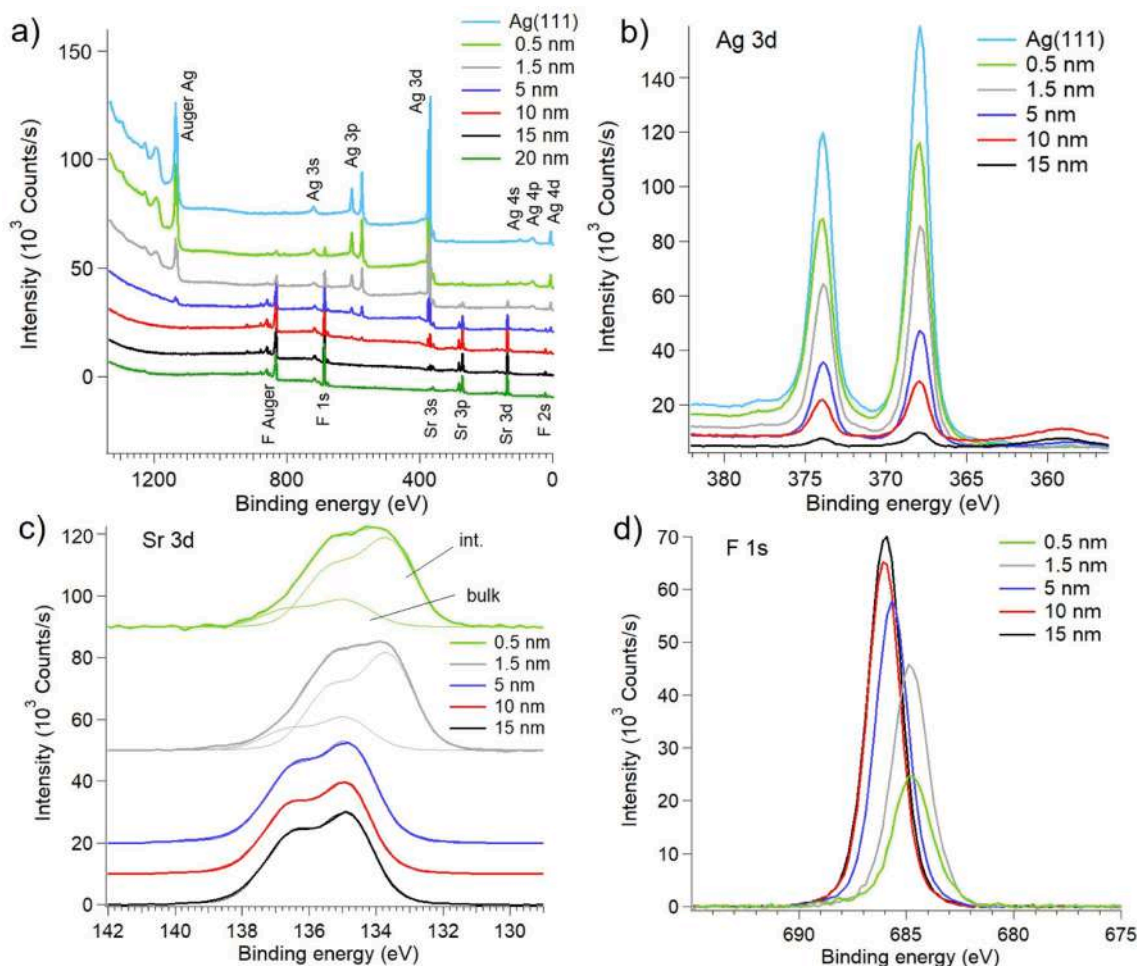
Fig. 7. a) XPS wide scans taken as a function of film thickness (RT deposition); spectra were shifted vertically for better visualization; b) Ag 3d levels; c) evolution of Sr 3d levels fitted with Voigt doublet components. For a clearer identification of the components, spectra have been normalised to the same maximum intensity; d) F 1s levels taken as a function of thickness.

3.2.2. High temperature growth

The film growth at higher temperatures, respectively 250 °C and 400 °C, was also investigated using UPS and XPS. The latter does not provide any additional or different information with respect to the data recorded at RT. Thus, the results are not shown here.

Fig. 8 reports the UPS electron distribution curves of the valence band of the $SrF_2/Ag(111)$ system at different coverages up to 5 nm, deposited at 250 °C (Fig. 8a) and at 400 °C (Fig. 8b). The overall spectra look similar to the RT case shown in Fig. 5, except that the features of the Ag 4d states remain visible up to 5 nm; the effect is more pronounced with increasing substrate temperature. This is consistent with the AFM data of Fig. 3 and Fig. 4, which show that portions of the surface remain uncovered (Fig. 4b) after high temperature growth. In particular, at 400 °C the triangular fluoride islands cover approximately the 76 % of the total surface, leaving relatively large areas of the surface as bare Ag (1 1 1), which explains the intense emission from the Ag 4d states of the clean surface, even at 5 nm of coverage (Fig. 8b).

4. Discussion

The growth mode of SrF_2 on Ag(1 1 1) in many aspects reflects the growth of other ionic fluorides on metals [22,23,47]: the fluoride does not wet the substrate and no strong chemical reactions take place between the interfacial fluoride atoms and the substrate. The fluoride tends to aggregate in islands with dendritic shapes at RT and low coverage, with some degree of decoration of the steps at adjacent terraces of the substrate. It is known that the steps of substrate terraces represent a barrier for surface diffusion [22]. The fluoride islands progressively extend laterally with increasing deposition time. At RT this results in the development of a relatively uniform film composed of coalesced crystallites that cover the substrate at 5 nm of nominal coverage. The film appears relatively flat and crystalline with the [1 1 1] direction perpendicular to the interface and twinned orientations of the lattice with respect to the Ag(1 1 1) substrate. At coverages thicker than 5 nm a band of filled electronic states develops in the fluoride gap. This is presumably associated with defects states (i.e. at step edges and at boundaries between the merging crystallites) that increase with the progressive growth of the film. The increase of the substrate temperature during deposition affects the growth mode in the sense that the fluoride islands tend to aggregate faster in larger crystallites that keep the (1 1 1) orientation of the substrate and are of a triangular prismatic shape. The weak interaction with the substrate favours 3D growth, with large portions of the surface left uncovered.

From the simulation of the RHEED patterns it is possible to derive the epitaxial relation with the substrate. A schematic model is represented in Fig. 9 for the similar epitaxial growth at RT and that of the main epitaxial component at 400 °C. In Fig. 9, one of the two possible twinned domains (at 180° to each other) is shown.

In spite of the lattice mismatch, the preferential growth mode of the fluoride mimics the geometry of the substrate. In this case, along the [1 1 0] compact directions, three Ag-Ag interatomic distances (8.67 Å) correspond almost to two Sr-Sr distances (8.20 Å). This is illustrated in
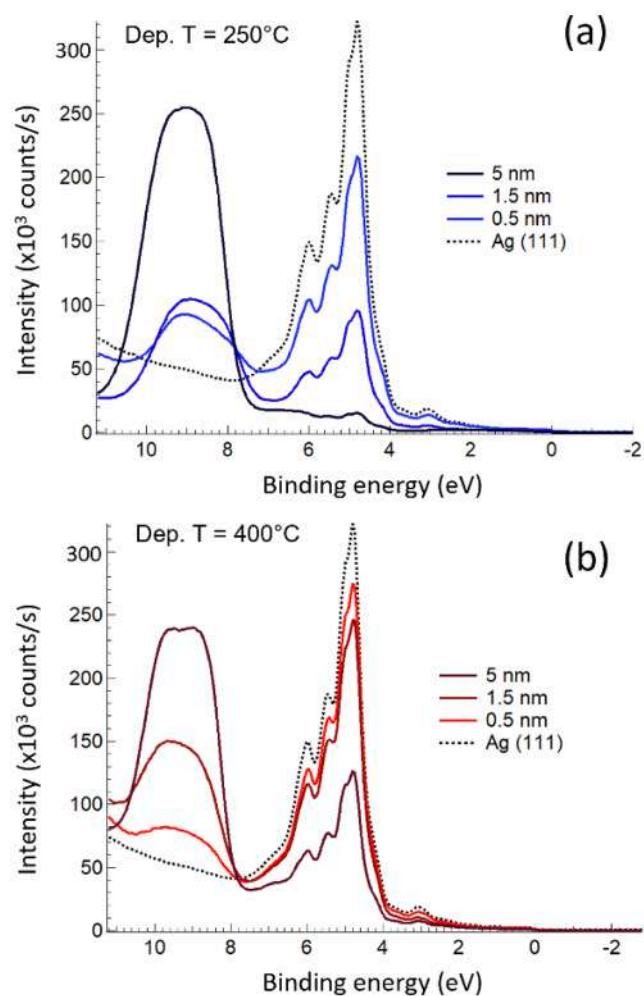
Fig. 8. UPS taken as a function of SrF$_2$ coverage: a) deposition at 250 °C, b) deposition at 400 °C.

Fig. 9.

In principle, we may note that better matching conditions could eventually be obtained by adopting an evaporation of mixed fluorides. The lattice constant of mixed Ca-Sr-Ba fluorides can in fact be tuned continuously from 5.46 to 6.20 Å, by adjusting the composition [55]. However, this is outside the scope of the present work.

From the UPS spectra it is also possible to derive the valence band offset of the fluoride with respect to the Ag metal. This can be obtained by linear extrapolation of the low binding energy slope of the F 2p structure in Fig. 5. For 5 nm of nominal coverage (before the development of the gap states and neglecting the shoulder at low binding energy associated with surface contributions) this gives a value of 6.7 eV.

5. Conclusions

Using atomic force microscopy, high energy electron diffraction and photoelectron spectroscopy supported by DFT calculations, we have investigated the growth mode, the chemical composition and the valence electronic properties of ultrathin layers of SrF$_2$ grown on Ag (1 1 1). SrF$_2$ was grown by molecular beam epitaxy in UHV at different substrate temperatures, from room temperature to 400 °C. It is observed that the stoichiometry of the fluoride is preserved right from the beginning of the deposition and independently of the substrate temperature. Both first principles calculations and electron spectroscopy results indicate that the interaction at the interface between the two materials is weak, without the formation of strong chemical bonds. At room temperature, the fluoride initially grows in the form of dendritic islands which soon coalesce and at 5 nm form a continuous film that covers the substrate. The film appears as being composed of twinned crystallites that preserve the (1 1 1) orientation of the substrate. In this sense, the ultrathin layers of SrF$_2$ on the Ag(1 1 1) single crystal, which in turn is grown on a mica support as in the present case, could be proposed as viable metal–insulator systems for the fabrication of ultrathin FET devices based on 2D semiconductors [8]. For the 5 nm film a band offset of 6.7 eV of the fluoride with respect to the metal is derived. When growth is carried out on heated substrates, the fluoride islands coalesce more rapidly, giving rise to 3D growth that leaves large portions of the substrate uncovered. At the temperature of 400 °C, besides (1 1 1)-oriented flat triangular prismatic islands that prevail at the surface, also (0 0 1)-oriented and vertically-developed crystallites are observed, which give rise to specific 3D diffraction spots in electron diffraction
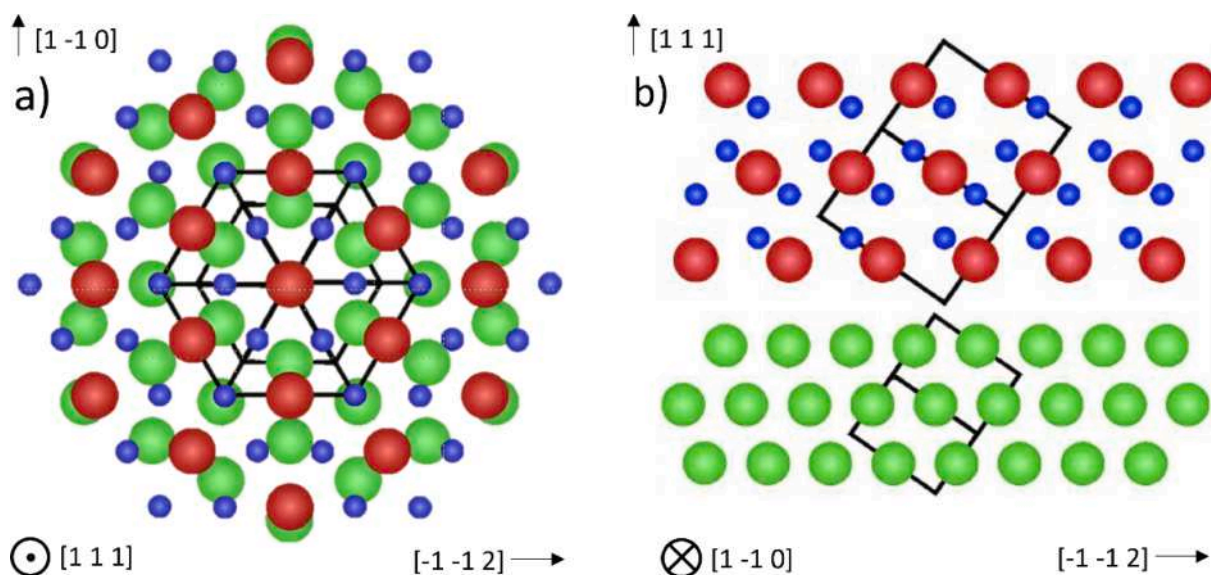

Fig. 9. a) top and b) side view of the SrF$_2$ lattice orientation (Sr red and F blue spheres) with respect to Ag(1 1 1) (green spheres). (For interpretation of the references to colour in this figure legend, the reader is referred to the web version of this article.)

measurements.

CRediT authorship contribution statement

Mauro Borghi: Writing – review & editing, Writing – original draft, Validation, Methodology, Investigation, Formal analysis, Data curation, Conceptualization. **Andrea Mescola:** Writing – review & editing, Methodology, Investigation, Formal analysis, Data curation. **Guido Paolicelli:** Writing – review & editing, Methodology, Investigation, Formal analysis, Data curation. **Monica Montecchi:** Investigation, Data curation. **Sergio D'Addato:** Writing – review & editing, Validation, Methodology, Conceptualization. **Simone Vacondio:** Writing – review & editing, Writing – original draft, Methodology, Investigation, Formal analysis, Data curation. **Luca Bursi:** Writing – review & editing, Writing – original draft, Methodology, Investigation, Formal analysis, Data curation, Conceptualization. **Alice Ruini:** Writing – review & editing, Writing – original draft, Validation, Supervision, Methodology, Funding acquisition, Data curation, Conceptualization. **Bryan P. Doyle:** . **Tibor Grasser:** Writing – review & editing, Validation, Supervision, Resources, Methodology, Funding acquisition, Conceptualization. **Luca Pasquali:** Conceptualization, Data curation, Formal analysis, Funding acquistion, Investigation, Methodology, Project administration, Supervision, Writing - original draft, Writing - review & editing.

Declaration of competing interest

The authors declare that they have no known competing financial interests or personal relationships that could have appeared to influence the work reported in this paper.

Data availability

Data will be made available on request.

Acknowledgements

References

[1] D. Akinwande, C. Huyghebaert, C.H. Wang, M.I. Serna, S. Goossens, L.J. Li, H.S. P. Wong, F.H.L. Koppens, Graphene and two-dimensional materials for silicon technology, Nature. 573 (2019) 507–518, https://doi.org/10.1038/s41586-019-1573-9.

[2] D.K. Polyushkin, S. Wachter, L. Mennel, M. Paur, M. Paliy, G. Iannaccone, G. Fiori, D. Neumaier, B. Canto, T. Mueller, Analogue two-dimensional semiconductor electronics, Nat. Electron. 3 (2020) 486–491, https://doi.org/10.1038/s41928-020-0460-6.

[3] H. Yu, M. Liao, W. Zhao, G. Liu, X.J. Zhou, Z. Wei, X. Xu, K. Liu, Z. Hu, K. Deng, S. Zhou, J.A. Shi, L. Gu, C. Shen, T. Zhang, L. Du, L. Xie, J. Zhu, W. Chen, R. Yang, D. Shi, G. Zhang, Wafer-Scale Growth and Transfer of Highly-Oriented Monolayer MoS2 Continuous Films, ACS Nano. 11 (2017) 12001–12007, https://doi.org/10.1021/acsnano.7b03819.

[4] K. Kang, S. Xie, L. Huang, Y. Han, P.Y. Huang, K.F. Mak, C.J. Kim, D. Muller, J. Park, High-mobility three-atom-thick semiconducting films with wafer-scale homogeneity, Nature. 520 (2015) 656–660, https://doi.org/10.1038/nature14417.

[5] IRDS, International Roadmap for Devices and Systems (IRDS), Ieee. (2021) 1–55. https://irds.ieee.org/editions/2020 (accessed September 1, 2023).

[6] C. Wen, M. Lanza, Calcium fluoride as high-k dielectric for 2D electronics, Appl. Phys. Rev. 8 (2021), https://doi.org/10.1063/5.0036987.

[7] Y.Y. Illarionov, T. Knobloch, M. Jech, M. Lanza, D. Akinwande, M.I. Vexler, T. Mueller, M.C. Lemme, G. Fiori, F. Schwierz, T. Grasser, Insulators for 2D nanoelectronics: the gap to bridge, Nat. Commun. 11 (2020) 1–15, https://doi.org/10.1038/s41467-020-16640-8.

[8] Y.Y. Illarionov, A.G. Banshchikov, D.K. Polyushkin, S. Wachter, T. Knobloch, M. Thesberg, L. Mennel, M. Paur, M. Stöger-Pollach, A. Steiger-Thirsfeld, M. I. Vexler, M. Waltl, N.S. Sokolov, T. Mueller, T. Grasser, Ultrathin calcium fluoride insulators for two-dimensional field-effect transistors, Nat. Electron. 2 (2019) 230–235, https://doi.org/10.1038/s41928-019-0256-8.

[9] A.I. Kingon, J.P. Maria, S.K. Streiffer, Alternative dielectrics to silicon dioxide for memory and logic devices, Nat. 2000 4066799. 406 (2000) 1032–1038. https://doi.org/10.1038/35023243.

[10] A. Laturia, M.L. Van de Put, W.G. Vandenberghe, Dielectric properties of hexagonal boron nitride and transition metal dichalcogenides: from monolayer to bulk, Npj 2D Mater. Appl. 2018 21. 2 (2018) 1–7. https://doi.org/10.1038/s41699-018-0050-x.

[11] Y.Y. Illarionov, M.I. Vexler, V.V. Fedorov, S.M. Suturin, N.S. Sokolov, Electrical and optical characterization of Au/CaF2/p-Si(111) tunnel-injection diodes, J. Appl. Phys. 115 (2014) 223706, https://doi.org/10.1063/1.4882375/372412.

[12] S.M. Suturin, A.G. Banshchikov, N.S. Sokolov, S.E. Tyaginov, M.I. Vexler, Static current-voltage characteristics of Au/CaF2/n-Si(111) MIS tunneling structures, Semiconductors. 42 (2008) 1304–1308, https://doi.org/10.1134/S1063782608110110/METRICS.

[13] W.K. Liu, M.B. Santos, Thin Films: Heteroepitaxial Systems, Ser. Dir. Condens. Matter Phys. 15 (1999) 704, https://doi.org/10.1142/3715.

[14] Y. Gao, T. Tiedje, P.C. Wong, K.A.R. Mitchell, X-ray-absorption near-edge structure at the fluorine *K* edge in CaF 2 and BaF 2, Phys. Rev. B. 48 (1993) 15578–15583, https://doi.org/10.1103/PhysRevB.48.15578.

[15] M.A. Olmstead, R.I.G. Uhrberg, R.D. Bringans, R.Z. Bachrach, Photoemission study of bonding at the CaF 2 -on-Si(111) interface, Phys. Rev. B. 35 (1987) 7526–7532, https://doi.org/10.1103/PhysRevB.35.7526.

[16] D. Rieger, F.J. Himpsel, U.O. Karlsson, F.R. McFeely, J.F. Morar, J.A. Yarmoff, Electronic structure of the CaF 2 /Si(111) interface, Phys. Rev. B. 34 (1986) 7295–7306, https://doi.org/10.1103/PhysRevB.34.7295.

[17] R.M. Tromp, M.C. Reuter, Structure of the Si(111)-Ca F 2 Interface, Phys. Rev. Lett. 61 (1988) 1756–1759, https://doi.org/10.1103/PhysRevLett.61.1756.

[18] N.S. Sokolov, S.M. Suturin, V.P. Ulin, L. Pasquali, G. Selvaggi, S. Nannarone, Initial stages of MBE growth and formation of CaF2/Si(001) high-temperature interface, Appl. Surf. Sci. 234 (2004) 480–486, https://doi.org/10.1016/j.apsusc.2004.05.034.

[19] L. Pasquali, S.M. Suturin, V.P. Ulin, N.S. Sokolov, G. Selvaggi, A. Giglia, N. Mahne, M. Pedio, S. Nannarone, Calcium fluoride on Si(001): Adsorption mechanisms and epitaxial growth modes, Phys. Rev. B. 72 (2005) 45448, https://doi.org/10.1103/PhysRevB.72.045448.

[20] L. Pasquali, S. D'Addato, G. Selvaggi, S. Nannarone, N.S. Sokolov, S.M. Suturin, H. Zogg, Formation of CaF2 nanostructures on Si(001), Nanotechnology. 12 (2001) 403–408.

[21] L. Pasquali, S.M. Suturin, A.K. Kaveev, V.P. Ulin, N.S. Sokolov, B.P. Doyle, S. Nannarone, Interface chemistry and epitaxial growth modes of SrF2 on Si(001), Phys. Rev. B. 75 (2007) 075403, https://doi.org/10.1103/PhysRevB.75.075403.

[22] F. Calleja, J.J. Hinarejos, A.L. Vázquez De Parga, S.M. Suturin, N.S. Sokolov, R. Miranda, Epitaxial growth of CaF2(1 1 1) on Cu(1 1 1) visualized by STM, Surf. Sci. 582 (2005) 14–20, https://doi.org/10.1016/J.SUSC.2005.03.003.

[23] D. Farías, K.F. Braun, S. Fölsch, G. Meyer, K.H. Rieder, Observation of a novel nucleation mechanism at step edges: LiF molecules on Ag(1 1 1), Surf. Sci. 470 (2000) L93–L98, https://doi.org/10.1016/S0039-6028(00)00917-1.

[24] D.A. Luh, C.W. Liu, C.M. Cheng, K.D. Tsuei, C.H. Wang, Y.W. Yang, Single-crystalline silver films on mica, Thin Solid Films. 645 (2018) 215–221, https://doi.org/10.1016/J.TSF.2017.10.051.

[25] D. Nazzari, J. Genser, V. Ritter, O. Bethge, E. Bertagnolli, G. Ramer, B. Lendl, K. Watanabe, T. Taniguchi, R. Rurali, M. Kolíbal, A. Lugstein, Highly Biaxially Strained Silicene on Au(111), J. Phys. Chem. C. 125 (2021) 9973–9980, https://doi.org/10.1021/ACS.JPCC.0C11033/ASSET/IMAGES/LARGE/JP0C11033_0003.JPEG.

[26] F. Tumino, C. Grazianetti, C. Martella, M. Ruggeri, V. Russo, A. Li Bassi, A. Molle, C.S. Casari, Hydrophilic Character of Single-Layer MoS2Grown on Ag(111), J. Phys. Chem. C. 125 (2021) 9479–9485, https://doi.org/10.1021/ACS.JPCC.1C01768/ASSET/IMAGES/LARGE/JP1C01768_0003.JPEG.

[27] D. Solonenko, O. Selyshchev, D.R.T. Zahn, P. Vogt, Oxidation of Epitaxial Silicene on Ag(111), Phys. Status Solidi. 256 (2019) 1800432, https://doi.org/10.1002/PSSB.201800432.

[28] S.M. Suturin, A.M. Korovin, V.V. Fedorov, G.A. Valkovsky, M. Tabuchi, N. S. Sokolov, An advanced three-dimensional RHEED mapping approach to the diffraction study of Co/MnF2/CaF2/Si(001) epitaxial heterostructures, J. Appl. Crystallogr. 49 (2016) 1532–1543, https://doi.org/10.1107/S1600576716011407.

[29] P. Hohenberg, W. Kohn, Inhomogeneous electron gas, Phys. Rev. 136 (1964) B864, https://doi.org/10.1103/PHYSREV.136.B864/FIGURE/1/THUMB.

[30] W. Kohn, L.J. Sham, Self-consistent equations including exchange and correlation effects, Phys. Rev. 140 (1965) A1133, https://doi.org/10.1103/PhysRev.140.A1133.

[31] R.M. Dreizler, E.K.U. Gross, Density Functional Theory: An Approach to the Many-Body Problem, Springer-Verlag, Berlin Heidelberg, 1990 http://doi.wiley.com/10.1002/9780470447710%5Cnhttp://link.springer.com/10.1007/978-3-642-86105-5 (accessed November 17, 2023).

[32] P. Giannozzi, S. Baroni, N. Bonini, M. Calandra, R. Car, C. Cavazzoni, D. Ceresoli, G.L. Chiarotti, M. Cococcioni, I. Dabo, A. Dal Corso, S. De Gironcoli, S. Fabris, G. Fratesi, R. Gebauer, U. Gerstmann, C. Gougoussis, A. Kokalj, M. Lazzeri, L. Martin-Samos, N. Marzari, F. Mauri, R. Mazzarello, S. Paolini, A. Pasquarello, L. Paulatto, C. Sbraccia, S. Scandolo, G. Sclauzero, A.P. Seitsonen, A. Smogunov, P. Umari, R.M. Wentzcovitch, QUANTUM ESPRESSO: a modular and open-source software project for quantumsimulations of materials, J. Phys. Condens. Matter. 21 (2009) 395502, https://doi.org/10.1088/0953-8984/21/39/395502.

[33] P. Giannozzi, O. Andreussi, T. Brumme, O. Bunau, M. Buongiorno Nardelli, M. Calandra, R. Car, C. Cavazzoni, D. Ceresoli, M. Cococcioni, N. Colonna, I. Carnimeo, A. Dal Corso, S. De Gironcoli, P. Delugas, R.A. Distasio, A. Ferretti, A. Floris, G. Fratesi, G. Fugallo, R. Gebauer, U. Gerstmann, F. Giustino, T. Gorni, J. Jia, M. Kawamura, H.Y. Ko, A. Kokalj, E. Kücükbenli, M. Lazzeri, M. Marsili, N. Marzari, F. Mauri, N.L. Nguyen, H.V. Nguyen, A. Otero-De-La-Roza, L. Paulatto, S. Poncé, D. Rocca, R. Sabatini, B. Santra, M. Schlipf, A.P. Seitsonen, A. Smogunov, I. Timrov, T. Thonhauser, P. Umari, N. Vast, X. Wu, S. Baroni, Advanced capabilities for materials modelling with Quantum ESPRESSO, J. Phys. Condens. Matter. 29 (2017) 465901, https://doi.org/10.1088/1361-648X/AA8F79.

[34] J.P. Perdew, K. Burke, M. Ernzerhof, Generalized Gradient Approximation Made Simple, Phys. Rev. Lett. 77 (1996) 3865, https://doi.org/10.1103/PhysRevLett.77.3865.

[35] M.J. van Setten, M. Giantomassi, E. Bousquet, M.J. Verstraete, D.R. Hamann, X. Gonze, G.M. Rignanese, The PseudoDojo: Training and grading a 85 element optimized norm-conserving pseudopotential table, Comput. Phys. Commun. 226 (2018) 39–54, https://doi.org/10.1016/J.CPC.2018.01.012.

[36] R.W.G. Wyckoff, Crystal structures, second ed., Interscience Publishers, New York, 1963.

[37] L.J. Sham, M. Schlter, Density-functional theory of the energy gap, Phys. Rev. Lett. 51 (1983), https://doi.org/10.1103/PhysRevLett.51.1888.

[38] J.P. Perdew, M. Levy, Physical content of the exact kohn-sham orbital energies: band gaps and derivative discontinuities, Phys. Rev. Lett. 51 (1983) 1884, https://doi.org/10.1103/PhysRevLett.51.1884.

[39] J.P. Perdew, R.G. Parr, M. Levy, J.L. Balduz, Density-Functional Theory for Fractional Particle Number: Derivative Discontinuities of the Energy, Phys. Rev. Lett. 49 (1982) 1691, https://doi.org/10.1103/PhysRevLett.49.1691.

[40] R. Jia, H. Shi, G. Borstel, Ab initio calculations for SrF2 with F- and M-centers, Comput. Mater. Sci. 43 (2008) 980–988, https://doi.org/10.1016/J.COMMATSCI.2008.02.012.

[41] G.W. Rubloff, Far-Ultraviolet Reflectance Spectra and the Electronic Structure of Ionic Crystals, Phys. Rev. B. 5 (1972) 662, https://doi.org/10.1103/PhysRevB.5.662.

[42] A. Balderschi, S. Baroni, R. Resta, Band Offsets in Lattice-Matched Heterojunctions: A Model and First-Principles Calculations for GaAs/AlAs, Phys. Rev. Lett. 61 (1988) 734, https://doi.org/10.1103/PhysRevLett.61.734.

[43] Y. Kumagai, K.T. Butler, A. Walsh, F. Oba, Theory of ionization potentials of nonmetallic solids, Phys. Rev. B. 95 (2017) 125309, https://doi.org/10.1103/PHYSREVB.95.125309/FIGURES/10/MEDIUM.

[44] A.J. Logsdail, D.O. Scanlon, C.R.A. Catlow, A.A. Sokol, Bulk ionization potentials and band alignments from three-dimensional periodic calculations as demonstrated on rocksalt oxides, Phys. Rev. B - Condens. Matter Mater. Phys. 90 (2014) 155106, https://doi.org/10.1103/PHYSREVB.90.155106/FIGURES/3/MEDIUM.

[45] G. Cappellini, A. Bosin, G. Serra, J. Furthmüller, F. Bechstedt, S. Botti, Electronic and Optical Properties of Small Metal Fluoride Clusters, ACS Omega. 5 (2020) 13268–13277, https://doi.org/10.1021/ACSOMEGA.0C01317/ASSET/IMAGES/LARGE/AO0C01317_0005.JPEG.

[46] B. Lüssem, S. Karthäuser, H. Haselier, R. Waser, The origin of faceting of ultraflat gold films epitaxially grown on mica, Appl. Surf. Sci. 249 (2005) 197–202, https://doi.org/10.1016/j.apsusc.2004.11.082.

[47] A.E. Candia, L. Gómez, R.A. Vidal, J. Ferrón, M.C.G. Passeggi, An STM and Monte Carlo study of the AlF3 thin film growth on Cu(1 1 1), J. Phys. D. Appl. Phys. 48 (2015) 265305, https://doi.org/10.1088/0022-3727/48/26/265305.

[48] L. Pasquali, S. Nannarone, M. Canepa, E.M. Staicu-Casagrande, V.A. Esaulov, Chlorine-induced modifications in the electronic structure of Ag surfaces: A metastable deexcitation spectroscopy and photoemission comparative study, J. Phys. Condens. Matter. 15 (2003) 3505–3516, https://doi.org/10.1088/0953-8984/15/21/301.

[49] J.G. Nelson, S. Kim, W.J. Gignac, R.S. Williams, J.G. Tobin, S.W. Robey, D.A. Shirley, High-resolution angle-resolved photoemission study of the Ag band structure along, Phys. Rev. B. 32 (1985) 3465–3471, https://doi.org/10.1103/PhysRevB.32.3465.

[50] W. Weiss, H.D. Wiemhöfer, W. Göpel, Role of ionic defects at semiconductor-insulator interfaces: Spectroscopic results on CaF2/InP(001) and SrF2/InP(001) structures, Phys. Rev. B. 45 (1992) 8478–8489, https://doi.org/10.1103/PhysRevB.45.8478.

[51] L. Pasquali, P. Fantini, S. Nannarone, M. Canepa, L. Mattera, Reactive and unreactive interfaces studied by means of metastable deexcitation spectroscopy, Surf. Sci. 352 (1996) 383–386.

[52] S. Tanuma, C.J. Powell, D.R. Penn, Calculations of electron inelastic mean free paths (IMFPS). IV. Evaluation of calculated IMFPs and of the predictive IMFP formula TPP-2 for electron energies between 50 and 2000 eV, Surf. Interface Anal. 20 (1993) 77–89. https://doi.org/10.1002/sia.740200112.

[53] V.M. Bermudez, Study of adsorption on radiation-damaged CaF2(111) surfaces, Appl. Surf. Sci. 161 (2000) 227–239, https://doi.org/10.1016/S0169-4332(00)00300-7.

[54] H.J. Wen, M. Daehne-Prietsch, A. Bauer, I. Manke, G. Kaindl, Stability of CaF2/Si (111) and Al/CaF2/Si(111) interface systems studied with photoelectron spectroscopy and scanning-tunneling microscopy, J. Vac. Sci. Technol. B Microelectron. Nanom. Struct. Process. Meas. Phenom. 13 (1995) 1645–1652, https://doi.org/10.1116/1.587872.

[55] M. Sugiyama, M. Oshima, MBE growth of fluorides, Microelectronics J. 27 (1996) 361–382, https://doi.org/10.1016/0026-2692(95)00062-3.